Science yield estimate with the Wide-Field Infrared Survey Telescope coronagraph

Wesley A. Traub
James Breckinridge
Thomas P. Greene
Olivier Guyon
N. Jeremy Kasdin
Bruce Macintosh

Science yield estimate with the Wide-Field Infrared Survey Telescope coronagraph

Wesley A. Traub,[a,*] James Breckinridge,[b] Thomas P. Greene,[c] Olivier Guyon,[d] N. Jeremy Kasdin,[e] and Bruce Macintosh[f]

[a]Jet Propulsion Laboratory, California Institute of Technology, M/S 321-100, 4800 Oak Grove Drive, Pasadena, California 91109, United States
[b]California Institute of Technology, M/S 105-50, 1200 East California Boulevard, Pasadena, California 91125, United States
[c]NASA Ames Research Center, MS 245-6, Moffett Field, California 94035, United States
[d]University of Arizona, Steward Observatory & College of Optical Sciences, 933 North Cherry Avenue, Tucson, Arizona 85721, United States
[e]Princeton University, C234 Engineering Quadrangle, Princeton, New Jersey 08544, United States
[f]Stanford University, Kavli Institute for Particle Astrophysics and Cosmology, Varian Physics Building, 382 Via Pueblo Mall, Stanford, California 94305, United States

Abstract. The coronagraph instrument (CGI) on the Wide-Field Infrared Survey Telescope will directly image and spectrally characterize planets and circumstellar disks around nearby stars. Here we estimate the expected science yield of the CGI for known radial-velocity (RV) planets and potential circumstellar disks. The science return is estimated for three types of coronagraphs: the hybrid Lyot and shaped pupil are the currently planned designs, and the phase-induced amplitude apodizing complex mask coronagraph is the backup design. We compare the potential performance of each type for imaging as well as spectroscopy. We find that the RV targets can be imaged in sufficient numbers to produce substantial advances in the science of nearby exoplanets. To illustrate the potential for circumstellar disk detections, we estimate the brightness of zodiacal-type disks, which could be detected simultaneously during RV planet observations. © *2016 Society of Photo-Optical Instrumentation Engineers (SPIE)* [DOI: 10.1117/1.JATIS.2.1.011020]

Keywords: coronagraphs; exoplanets; direct imaging; spectra; disks.

Paper 15052SS received Jun. 15, 2015; accepted for publication Feb. 22, 2016; published online Mar. 18, 2016.

1 Introduction

The Wide-Field Infrared Survey Telescope (WFIRST) is the top-priority large space mission identified in the 2010 National Academy of Sciences decadal survey, New Worlds New Horizons. With the transfer to NASA of the astrophysics focused telescope assets (AFTA), and the decision to use one of these telescopes to implement WFIRST, the resulting mission, then known as WFIRST-AFTA and subsequently shortened to WFIRST in early 2016, will be able to directly image exoplanets and circumstellar disks, as we discuss in this paper.

The mission was described in a report[1] by the Science Definition Team and WFIRST Study Office. The mission envisioned in that report uses the repurposed 2.4-m AFTA telescope equipped with a wide-field instrument (WFI) comprising a wide-field camera with a field of view 200 times larger than the Hubble Space Telescope (HST) WFC3 camera, with an integral field unit, which will characterize supernovae to trace the evolution of the universe. The WFI will also use gravitational microlensing to discover orbiting as well as free-floating exoplanets that will complement those already known from the Kepler mission.

In addition, the mission includes a coronagraph instrument (CGI), which will be the first instrument capable of directly imaging and characterizing giant and sub-Neptune-size planets around nearby Sun-like stars. The mission addresses all three of the questions identified for astrophysics in the NASA 2014 Science Plan: "How does the universe work?", "How

did we get here?", and "Are we alone?" The mission entered Phase A in February 2016. In this paper, we provide our preliminary estimate of the science yield of the CGI for two classes of objects: the known radial-velocity (RV) planets and the debris disks around nearby stars.

1.1 Expected Science Gains

The views of planetary systems known today are constrained by opportunistic situations, for example, planets that are massive enough to induce a measurable RV reflex motion in their stars, planets that transit their stellar disk, planets that are self-luminous owing to their extreme youth, or planets that lie far enough from their star that the speckle halo can be subtracted. Images from the WFIRST CGI will allow us to go well beyond these special circumstance cases. We will see planets that have the full range of orbital inclinations, planets of all ages shining by the reflected light of their star, and planets that lie in the few-astronomical unit semimajor axis range. In other words, we will be able to image planetary systems that are more like our solar system.

This paper focuses mainly on known RV planets simply because they are known; therefore, we have a reasonable expectation of being able to anticipate their signal levels. However, two other classes of targets for the CGI are dust disks and new-discovery planets, which we will touch on, but because of their unknown signal strengths, we cannot confidently predict their frequency or detectability.

---

*Address all correspondence to: Wesley A. Traub, E-mail: wtraub@jpl.nasa.gov

The expected science gains from known RV planet images and spectra are numerous and have been addressed in several studies carried out specifically for the CGI by Burrows, Hu, and Marley et al.,[2–4] as well as for dust disks by Schneider.[5] In short, CGI images of a planet, in a single filter, will provide projected orbit vectors, which, with adequate RV information, will allow us to estimate the orbital inclination angle, and hence the planet's mass.[6] Planet images in two or three filters can lead to color information, which can be interpreted in terms of planetary type, such as gas giant, ice giant, exposed rock surface, thick Rayleigh scattering atmosphere, and so on.[7] Planet spectra, for giants, can give us information on atmospheric structure and molecular composition, cloud layers, cloud coverage, and metallicity.[2–4] For circumstellar disks, images of nonuniform brightness may be able to tell us about unseen sources and sinks of dust, such as comet or asteroid families or planets, and colors and polarization can tell us about dust grain sizes.[5]

In all cases, the degree to which we can infer physical properties will depend on the signal-to-noise ratio (SNR) of the observations, which is the focus of the present paper. The size of telescope and the efficiency of its coronagraph are critical parameters, so a key goal of this paper is to understand the expected performance of the flight system as currently envisioned, before we begin to freeze the design and while there is time to consider instrumental trade-offs. For this purpose, it is sufficient to focus on the known RV planets. Future studies should consider a broader science range, including dust disks and new-discovery planets, as well as increasingly realistic design reference missions (DRMs).

1.2 Comparison to Other Studies

For context, we note that there are several recent studies of the detectability of nearby exoplanets, and of the science that could result. Two of these studies refer to unique non-WFIRST architectures; therefore, they explore a different portion of parameter space, specifically the class of missions that potentially could be carried out for less than a billion dollars, labeled "probe" missions. One of these, the Exo-C mission,[8] a 1.4-m-diameter clear-aperture telescope with an internal coronagraph, is based on a design very similar to the hybrid Lyot coronagraph (HLC) in the present paper. The other, the Exo-S mission,[9] is a 1.1-m-diameter telescope with a 30-m-diameter starshade at a distance of ~25,000 to 39,000 km, as well as a version of it that uses the WFIRST telescope at L2, with a larger starshade. A separate paper consistently comparing these missions, including the CGI, is in preparation.[10]

Two other studies looked at DRMs based on telescopes larger than WFIRST, in anticipation of an even more capable generation of exoplanet-finding telescopes, which could follow WFIRST, and these are of interest for context. The first of these is a paper by Stark et al.,[11] and the second is a paper by Brown.[12] Both papers provide DRM studies of parameterized telescopes, with diameters in the 8- to 16-m class, with idealized coronagraphs and exoplanet populations, but applied to real stars, using observing scenarios optimized to maximize the yield of planet detections. These studies are valuable in showing the relative importance of parameters such as telescope diameter and coronagraph inner working angle (IWA), but we caution that the nonlinear nature of the discovery yield process and the choice of parameter values (efficiencies, and so on) suggest that the absolute values of the resulting quantities (e.g., telescope diameter)

should be reexamined when specific engineering designs for an actual mission are available.

An estimate of a planet's mass can be obtained from direct imaging combined with RV data, although, as Brown[6] points out, the accuracy of the mass estimate is limited by the number and quality of the images. We do need to know the mass and radius in order to derive surface gravity and albedo, which in turn leads to a better understanding of spectra; however, it is beyond the scope of this paper to estimate the accuracies and interplay of these quantities.

1.3 Unique Aspects of the Present Study

The present study is unique in that it addresses a specific engineering design for three types of coronagraphs, each coupled to a specific telescope. The only parameters to vary are those of the coronagraphs themselves, and to a large extent, they have already been optimized to yield the maximum number of RV planet detections with the given WFIRST telescope. This is a quantitatively different situation than the parameter-based studies mentioned above, in the sense that the exoplanet yield is a nonlinear function of many parameters. To be specific, engineering factors, such as the following, are very important controlling factors in determining exoplanet yields in an actual instrument: (1) the degree to which planet photons are focused in an image core (surprisingly low, owing indirectly to the complex pupil), (2) the degree to which the star image can be stabilized in spite of telescope pointing jitter (again, a critical factor that depends on specific hardware), and (3) the wavefront distortion caused by telescope-induced polarization (forcing the selection of a single polarization in the detector plane, thereby reducing the photon collection rate by a factor of two of the coronagraphs in this study). The present study takes into account all of the specific instrument parameters expected with WFIRST, so to this extent, the present study is different from previous studies. The conclusions may differ as well, owing in part to the nonlinear nature of the problem.

2 Target Planet and Star Brightness

In this section, we provide the information needed to calculate photon fluxes from target stars and their planets.

2.1 Radial Velocity Planet Catalog

The list of known RV planets used here was obtained from the Exoplanet Orbit Database at Penn State University,[13] on September 12, 2015, by downloading the "RV planets" option and including relevant stellar parameters for reference. After eliminating stars with missing distance or V magnitude entries, and keeping only those with a planet–star separation $\beta > 0.040$ arc sec (see Sec. 2.3), the list contains 127 targets. Each target has a measured $m \sin(i)$ value, which we take to be the approximate mass of the planet, given that the statistically expected value of $\sin(i)$ is ~0.79.

None of these planets has a measured radius, so a radius $r(m)$ was assigned using an empirical relation from Ref. 14.

$$r(m) = 0.22 + 14.0/\{1 + [|\log(m/600)|/1.15]^{3.31}\},$$

where the absolute value of the log term is to be taken, the log is base 10, and the mass m and radius r are both in Earth units. This relation was obtained from a least-squares fit of known mass and radius values to a curve that has the general shape

expected of a cold, gravitationally bound body, and is shown as a smooth curve in Fig. 1, with the assigned radius values at each RV-inferred mass value superposed as small blue circles on the curve. The scattered red circles in Fig. 1 are observed planets that have had both mass and radius measured. Clearly, there is scatter in the data, on the order of ~13% (cf. Sec. 2.4), so the empirically assigned radii also should be considered to be uncertain by about the same amount. It is clear from the clustering of inferred RV radius points near a value of about one Jupiter radius that most of the RV planets are gas giants, with a smaller number falling in the Neptune radius range.

2.2 Star Brightness

The host stars for the 127 RV planets in the present study all have a listed V magnitude, but are missing a blue magnitude minus visible magnitude (B-V) color, so this was supplied using the following empirical fit to data from Appendix C of Ref. 15:

$$B - V(mag) = 15.79 - 4.02 \times \log_{10}(T_{eff}).$$

This expression is accurate to better than 0.1 mag, and valid for $T_{eff} < 8000$ K, which includes all target stars in the present study.

To obtain the photon rate, we use the following empirical expressions, obtained from examination of the tables in Ref. 15 (Appendix C), and using the formalism for $f(\lambda, m)$ in Ref. 16:

$$f(\lambda, m) = 10^{a(\lambda) - 0.4 * m(\lambda)} \text{ photons/(s cm}^2 \text{ nm)},$$

$$a(\lambda) = 4.01 - (\lambda - 0.55)/0.77 \text{ mag},$$

$$m(\lambda) = V + b * (B - V) * (1/\lambda - 1.818) \text{ mag}.$$

Here, λ is in units of μm, and the range of validity is 0.4 μm $< \lambda <$ 1.0 μm. The slope factor is

$b = 2.20$ if $\lambda < 0.55$ μm, $\quad b = 1.54$ if $\lambda > 0.55$ μm.

The expression for flux, $f(\lambda, m)$, is accurate to ~7%, in the stated range of λ.

2.3 Planet Brightness

The planet's illumination geometry is estimated for a circular orbit, an average orbital inclination $i = 60$ deg with respect to an edge-on orbit, and an angular anomaly $\theta = 70$ deg in the plane of the orbit, measured with respect to superior conjunction. A circular orbit is chosen because the actual orbits are roughly circular, with a median eccentricity of 0.21. The inclination angle is chosen to represent the statistical average of the as-yet unknown inclination. The angular position is chosen to represent a point in the orbit where the planet is expected to be relatively bright and relatively far from its star, i.e., it is slightly brighter than at maximum elongation, and slightly closer to the star in angular separation. This orbital location gives a phase angle α specified by $\cos(\alpha) = \sin(i) \times \cos(\theta)$, or $\alpha = 72.77$ deg, which in turn gives an angular separation on the sky of

$$\beta = \sin(\alpha) \times R/d,$$

which is smaller than maximum elongation by a factor $\sin(\alpha) = 0.96$, where R is the orbital radius and d is the distance to the star. In this paper, β ranges from a minimum of 0.040 arc sec, the inner working angle of one of the coronagraphs, to a maximum of 1.00 arc sec for epsilon Eri b. With this angular restriction, the list of planets drops from 264 down to 127 RV targets.

The planet brightness is estimated for a visible geometric albedo of $p = 0.50$, which is roughly the same as Jupiter's albedo in the range of 400 to 700 nm, and representative of Jupiter's continuum segments from 700 to 1000 nm, shown in Fig. 2. The planet's phase function Φ is taken to be a Lambert scattering function,
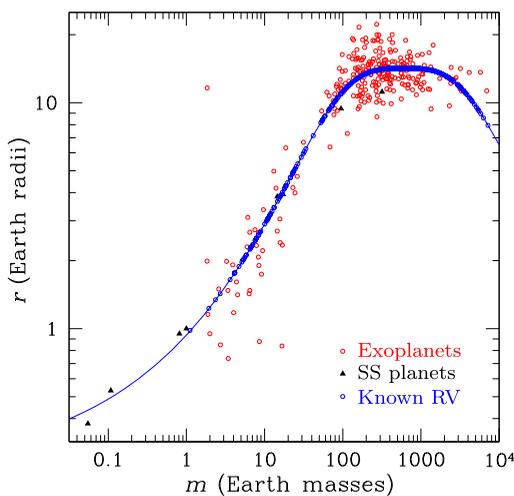

Fig. 1 The empirical radius of a planet is shown as a function of mass, by the blue curve, as given by the formula in the text. The mass values of the 460 known RV planets are projected onto this curve, and shown as small blue circles, from which point the inferred radii can be read. For comparison, the 264 exoplanets that have known values of radii as well as mass are shown as small red circles, and solar system objects are shown as black triangles.
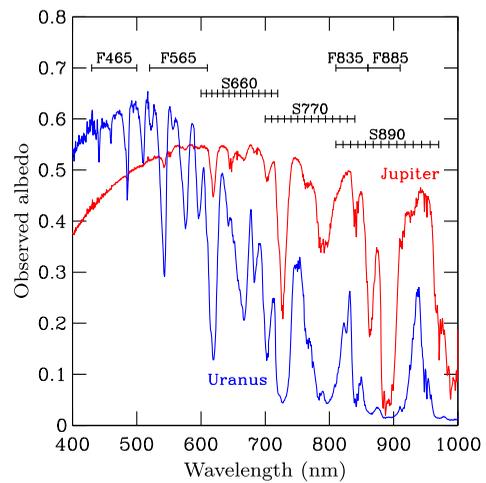

Fig. 2 Geometric albedo of Jupiter and Uranus,[17] showing the albedo as a function of wavelength, the characteristic widths of spectral features (nearly all CH_4), the four proposed filter locations and widths, and the three proposed spectrometer bands and resolution elements, drawn here at a resolution of $R = 70$, chosen to approximately match the widths of the narrowest features in these spectra, and therefore maximize the accuracy of inferred CH_4 mixing ratios.

$$\Phi(\alpha) = [\sin(\alpha) + (\pi - \alpha) \times \cos(\alpha)]/\pi,$$

since the precise phase function is unknown. We define the planet contrast C in the standard way as the ratio of the apparent brightness of the planet to that of the star, giving

$$C(\alpha) = p \times \Phi(\alpha) \times (r/R)^2,$$

where r is the planet radius and R is the planet–star distance (semimajor axis). The flux from the planet incident on the telescope is, of course, the star flux $f(\lambda)$ times the contrast $C(\alpha)$.

We show in Fig. 3 the estimated contrast of known RV planets, as a function of their angular separation as specified above, for the 127 RV planets that fall in the range of planet-star separation angles given above, i.e., $\beta > 0.040$ arc sec.

In this paper, we assume that the orbital period and phase are well known, allowing us to estimate the optimum calendar date on which to search for the planet. It is beyond the scope of this study to set requirements for the accuracy and frequency of precursor RV observations needed, and it is also outside the scope of this paper to carry out DRM studies to set requirements for the schedule of visits to a target, and the observational completeness (fraction of visits that result in a useful measurement). For a broad range of inclinations, with an up to date RV solution, it is possible to determine a range of dates over which the planet will have best observability (typically between 60 and 90 deg phase). The main remaining uncertainty is the position angle on the sky, which requires that the search range be able to cover 360 deg of azimuth, either in one observation or in sequential ones.

2.4 Uncertainty in Planet Contrast and Angular Separation

In this section, we estimate the relative uncertainty in the expected star–planet contrast C and star–planet angular separation β. This uncertainty is based on the planet-to-planet variations that might exist in nature, including albedo, diameter, eccentricity, and orbital orientation with respect to the observer; it is not an estimate of SNR, which we address in Sec. 4.10.

For RV planets, we already know the planet mass, semimajor axis, and eccentricity with a reasonable degree of accuracy.
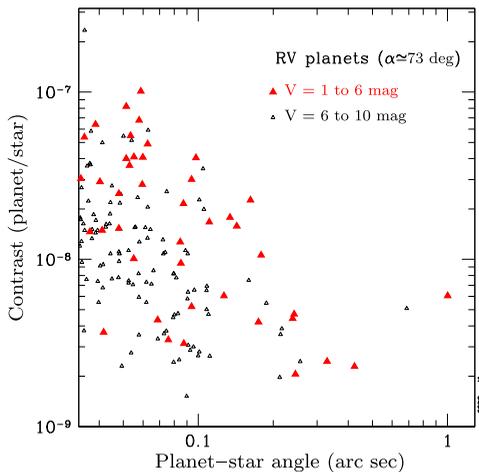

Fig. 3 Contrast versus angular separation for the 127 exoplanets in the RV catalog used in this paper, assuming circular orbits, $i = 60$ deg inclination, $\theta = 70$ deg orbital location, $p = 0.50$ visible albedo, and Lambert phase function.

From these known values, we can estimate the planet radius and brightness, and the relative uncertainties in all quantities, as follows.

The contrast is a function of albedo, phase function, planet radius, and orbit radius, as given above, where the latter is given by

$$R = a(1 - e^2)/[1 + e \cos(t)].$$

Here, e is the eccentricity and t is the true anomaly (angle from perihelion to instantaneous position). We note that the extremes of orbit radius are $R_{\max} = a(1 + e)$ and $R_{\min} = a(1 - e)$.

The relative uncertainty in contrast, $\Delta C/C$, is given by the differential approximation

$$\Delta C/C = \Delta p/p \oplus \Delta\Phi/\Phi \oplus 2\Delta r/r \oplus 2\Delta R/R,$$

where the $\oplus$ symbol indicates a root-sum-square operation, assuming that the quantities are statistically independent. Likewise, for the relative uncertainty in the angular separation $\Delta\beta/\beta$, we have

$$\Delta\beta/\beta = \Delta \sin(\alpha)/\sin(\alpha) \oplus \Delta R/R \oplus \Delta d/d.$$

We now proceed to estimate each of the contributing terms in these two equations. For albedo, the observations of solar system giant planets by Ref. 17 are useful as a guide to what might be expected for the RV exoplanets, which are dominantly Jupiter-mass objects, with a median semimajor axis value of ~ 3.3 AU. Karkoschka measured the visual spectra of Jupiter, Saturn, Uranus, and Neptune in 1993 and 1995, with statistical and systematic accuracies of better than 1 and 4%, respectively. He found that the time variation of full-disk magnitudes in the V, R', and I' bands for these four planets was ~ 0.012 magnitudes rms, or $\sim 1.2\%$. The full-disk albedos in a continuum region at 550 nm, in a 15% band, are estimated from Karkoschka's spectral plots to be ~ 0.52, 0.50, 0.60, and 0.54 (all times 1.05 to correct the values to full opposition) for Jupiter, Saturn (with the rings edge-on, so very little of the disk was shadowed), Uranus, and Neptune, respectively, giving an average of 0.567 and an rms scatter of ± 0.045. The relative uncertainty in exoplanet albedo is therefore taken to be $\Delta p/p \cong 0.079$.

We note that the albedo of a giant planet is expected to be as high as indicated above only for the case where the planet is sufficiently far from its star that water and ammonia clouds can form in the atmosphere. When the planet moves closer to its star, for example, for Jupiter, between ~ 0.8 and 2 AU from the Sun,[18] these clouds tend to be absent, owing to the atmospheric temperature exceeding the condensation temperature, so the incident starlight will not be reflected, rather it will penetrate deeper into the atmosphere, and will tend to be absorbed by molecular features such as those of CH_4, leading to a lower albedo for planets at these closer orbital radii (e.g., Ref. 2). We do not consider these lower albedos in this study because the inner working angle of the prime coronagraphs on WFIRST will preclude finding many such objects.

For the phase function Φ, the Lambert law is used, along with the relation for phase angle α in terms of orbital inclination i (angle between orbital plane and observer's sky) and angular anomaly θ.

$$\cos(\alpha) = \sin(i) \times \cos(\theta).$$

Since i is statistically distributed as $[1 - \cos(i)]$, the half-point occurs at $i = 60$ deg, and the width of the distribution is roughly from 0.25 to 0.75, or ± 17 deg. Inserting these values along with the selected orbital anomaly value of $\theta = 70$ deg (presumably known for RV planets) gives a phase function of $\sim 0.481 \pm 0.031$, for a relative uncertainty of $\Delta\Phi/\Phi \cong 0.064$.

For the planet radius r, the median difference between the individual radius values and the smooth curve in Fig. 1 is $\sim 13\%$, giving $\Delta r/r \cong 0.013$.

For the orbital radius R, we use the approximate relation

$$\Delta R/R \cong \Delta a/a \oplus a\Delta e$$

derived from the $R_{\min}$ and $R_{\max}$ relations (rather than using the exact relation above, which requires averaging over time and orbital orientations, and is therefore more complex than needed for present purposes). Then, for the semimajor axis a, we use the median observed uncertainty in the top 35 RV targets (those with nominal angular separations of 0.100 arc sec or greater) to find $\Delta a/a \cong 0.031$. Likewise, the median uncertainty in observed eccentricity is $\Delta e \cong 0.045$. The combined result is $\Delta R/R \cong 0.135$.

For the sine of the phase angle, we use the nominal angular anomaly θ and the range of inclinations to find $\Delta \sin(\alpha)/\sin(\alpha) \cong 0.016$. For the observer-star distance d, we use the median uncertainty in distance to the above set of RV targets to find $\Delta d/d \cong 0.008$. The combined result is a relative uncertainty in contrast of $\Delta C/C \cong 0.39$ and an uncertainty in angular separation of $\Delta\beta/\beta \cong 0.036$, as shown in Table 1. These values will be used in Figs. 8–10, where we plot the contrast versus separation for RV planets.

The large gap between the uncertainties owing to the combined effects of albedo, phase function, and semimajor axis, versus the uncertainty from planet radius, suggests that photometric measurements of the contrast of directly imaged planets might

be considered as evidence for planet radii, with the other parameters being inferred from the measured geometry of the system plus inferences of the planet albedo on the basis of model atmospheres, a possibility once suggested by Ref. 7, but shown here more quantitatively.

3 Coronagraph Instrument Model

The purpose of our CGI model is to predict the fraction of planet light incident on the telescope that is delivered to the focal plane detector, the shape of that spot [the point spread function (PSF)], the instrumental polarization distortion, the brightness of the background-diffracted speckles, and the degree to which the speckles vary with time. Our CGI model comprises four parts: a telescope model, a coronagraph model, a detector model, and a wavefront propagation model, all discussed in Sec. 3. In Sec. 4, we discuss the exoplanet detection algorithm, which uses these elements to calculate the exoplanet yield.

3.1 Telescope Model

Our telescope model comprises the shape of the pupil (including the central obscuration and six spider arms), the off-axis angle of the CGI, the mirror prescriptions, the model power spectral density (PSD) of phase and amplitude errors of the primary mirror and secondary mirror, the model root-mean-square (RMS) pointing jitter, the coating reflectivity as a function of wavelength, and the polarization transformation as a function of wavelength and position within the pupil. In a separate calculation (not included in this paper, but relevant to our estimates of the time needed to create a dark hole), we use estimates of the model wavefront deformation owing to thermal changes in the shape and location of telescope mirrors, as a function of pointing angle, and recent slew angle history.

3.2 Coronagraph Model

Our coronagraph model includes the two coronagraph architectures that were chosen as the prime instrument after a community-wide downselection process in 2013, plus a third architecture as a study-phase backup.[19] The prime instruments are the HLC (Refs. 20 and 21) and the shaped pupil coronagraph (SPC).[22,23] The HLC and SPC are combined into a single package, the occulting mask coronagraph (OMC), in which operation in HLC or SPC mode is determined by the selection of a flip mirror. The backup instrument is the phase-induced amplitude apodization complex mask coronagraph (PIAACMC).[24,25]

The coronagraph data files in this paper are all for 550 nm and 10% bandwidth. The HLC design is from Moody on September 15, 2015, which in turn is a slightly improved version of a design from Moody and Krist on August 14, 2014, with the name 20140623-139, for a single polarization. The SPC design is from Krist on September 25, 2014, labeled 20140902-1, for unpolarized light. The PIAACMC design is from Guyon and Krist on March 26, 2015, labeled 20150322, or Gen3, for a single polarization.

All these architectures are currently (early 2016) being developed in parallel in the lab. Each uses a combination of phase and amplitude control of the wavefront, in the pupil, near-pupil, and image planes, to achieve contrast values on the order of 10^{-9} over a range of azimuthal and radial angles on the sky. The coronagraph systems feed both a direct imager and an integral field spectrometer (IFS).[26]

Table 1 Relative uncertainties in the contrast and separation of RV planets with respect to their parent stars, as estimated for the set of known RV planets accessible to the coronagraph on WFIRST. The contributing terms are also listed, for completeness.

Item name	Relative uncertainty	Value
Albedo	$\Delta p/p$	0.079
Phase function	$\Delta\Phi/\Phi$	0.064
Planet radius	$\Delta r/r$	0.130
Semimajor axis	$\Delta a/a$	0.031
Eccentricity	Δe	0.045
$a \times e$	$a \times \Delta e$	0.131
Orbit radius	$\Delta R/R$	0.135
Sine phase angle	$\Delta \sin(\alpha)/\sin(\alpha)$	0.016
Distance	$\Delta d/d$	0.008
Contrast	$\Delta C/C$	0.388
Angular separation	$\Delta\beta/\beta$	0.036

The status of the OMC in its lab testbed is that it has passed its scheduled milestones on time, including the most recent one (September 2015) of achieving a raw contrast of 10^{-8}, with a bandwidth of 10%, at a central wavelength of 550 nm, in a static environment. Its next milestone (September 2016) is the same but in a dynamic environment, which will include pointing jitter of the telescope.

The status of the PIAACMC is that its focal plane mask with at least 12 concentric rings has been fabricated and characterized, and that the results are consistent with model predictions of 10^{-8} raw contrast, with a bandwidth of 10%, at a central wavelength of 550 nm, all of which was for its most recent milestone (December 2014). Its next milestone (September 2016) is to demonstrate a raw contrast of 10^{-8}, with a bandwidth of 10%, at a central wavelength of 550 nm, in a static environment, and that its contrast sensitivity to pointing and focus is characterized.

In the present paper, we estimate coronagraph performance at wavelengths other than 550 nm, and bandwidths other than 10%, as specified in Ref. 1, and as will be displayed later in Table 2. We do this by scaling the 550-nm design by wavelength, assuming that the scaled designs can be implemented in the lab. We further assume that the 10% bandwidth can be extended to the bandwidths in Table 2, by appropriate design changes. Thus, the yield estimates in this paper are based on coronagraph designs that have yet to be created in the computer and implemented in the lab, but which we feel are achievable, based on past experience.

3.3 Detector Model

Our detector model is based on the well-known electron-multiplying CCD201 (EMCCD) from e2v.[27] Model parameters include pixel size, wavelength dependence of quantum efficiency, and parameters for each of the three read modes: ordinary CCD-type operation (zero gain), electron-multiplying analog operation, and electron-multiplying photon-counting operation. All three modes are accessible during flight, but for the present estimate, we use only the latter, most sensitive, photon-counting mode. Key

parameters of interest, as used in the current simulations, include dark current (0.0005 electrons/s per pixel), clock-induced charge (0.001 electrons per pixel per read), gain factor (500), read noise (16 electrons RMS per read), and integration time per snapshot (300 s).

3.4 Wavefront Propagation Model

Our wavefront propagation model is the PROPER program[28] employed for all of the instrument performance calculations in this section. PROPER propagates a scalar wavefront through all of the telescope and CGI optical surfaces, in the near and far fields, using Fourier-based Fresnel and angular spectrum methods. For the purpose of calculating science yield, the key results from PROPER are the azimuth-averaged contrast values of the background speckle field and the fraction of planet light in the core of the PSF as given by the area enclosed by the full-width at half-maximum (FWHM) of the focal-plane image of a point source on the sky. Values for these two parameters are calculated for each of the two orthogonal linear polarizations, as a function of radial angle on the sky, for (1) selected values of the RMS angular jitter of the telescope pointing direction, (2) a given PSD of polishing errors and amplitude errors on the telescope mirrors, (3) two values of the factor by which the speckle intensity can be reduced, and (4) the function integrated over the full wavelength band.

Polarization is accounted for by noting that the portion of the incident wavefront that is reflected from the angled mirrors (including the primary mirror) will suffer a phase delay between the radial and tangential components, which in turn negatively affects the coronagraph's performance. Therefore, we currently plan to separate the x and y polarizations with a Wollaston prism placed immediately in front of the direct-imaging detector; the coronagraph deformable mirror settings can be tuned to optimize contrast in either x or y polarization. The spectrograph may use either a single fixed polarizer or none; simulations show the SPC is less sensitive to these low-order differential aberrations. Thus, the dark hole will be achieved and the science measurements taken in one or both polarizations, depending on the science goals, and in all cases, both polarizations will be simultaneously recorded.

4 Exoplanet Detection Algorithm

The expected science yield of the CGI is estimated separately for each of the coronagraph architectures as follows. For each wavelength band, we estimate the count rate of electrons, in the FWHM of the planet image, for the given radial (sky) location of the planet, using the factors of transmission as well as image size and expected speckle contrast as supplied by PROPER, as explained in this section. We make this estimate for each of the three values of RMS pointing jitter (0.4, 0.8, and 1.6 mas), and for two values of postprocessing factor (1/10 and 1/30), where the latter parameter gives the factor by which we expect to reduce the RMS spatial variation of the speckle contrast (equal to the average contrast, owing to speckle statistics) by mathematical processing of the image data on the ground. This processing is an active area of study and is not discussed further in the present paper. We also estimate the noise associated with the detection of the planet image as the square root of the sum of the total electron count in the FWHM of the image (planet counts, speckle counts, detector counts, zodiacal background and foreground counts, all increasing with time) plus the fixed noise floor from the speckles reduced by the

Table 2 Science filter bands. For each filter, the columns give the central wavelength, ratio of FWHM to central wavelength, nominal science purpose, polarization state, destination focal plane, and coronagraph architecture to be used for that filter and destination. The filters are as listed in the WFIRST-AFTA report,[1] and as such are goals for technology development.

λ_0 (nm)	$\Delta\lambda_{FWHM}/\lambda_0$ (%)	Purpose	Polarization	Channel	Coron.
465	15.1	Continuum, Rayleigh	Pol.	Imager	HLC
565	15.9	Continuum, Rayleigh	Pol.	Imager	HLC
835	6.0	CH_4 continuum	Unpol.	Imager	SPC
885	5.6	CH_4 absorption	Unpol.	Imager	SPC
660	18.0	CH_4 spectrum	Unpol.	IFS	SPC
770	18.0	CH_4 spectrum	Unpol.	IFS	SPC
890	18.0	CH_4 spectrum	Unpol.	IFS	SPC

postproduction factor (not increasing with time). Each of these steps is discussed in the present section.

4.1 Transmission Factors Versus Wavelength

The wavelength-dependent instrument transmission factors, which are independent of the coronagraph, are shown in Fig. 4. Curve R_1 is the reflectivity of a single overcoated silver mirror, for a typical coating (FSS99-600, Ref. 29) at near-normal incidence. Curve R_{32} is the reflectivity of 32 such mirrors, i.e., $R_{32} = R_1^{32}$, where the value of 32 is from a recent stage of design of the CGI. The curve QE is a typical quantum efficiency of the CCD201-20 detector at $-20°C$, with a midband coating (e2v data sheet). The curve T_{area} is the geometric transmission factor of the telescope's spiders and central obscuration, compared to a 2.4-m clear aperture. The T_{fil} curve is an estimated transmission factor comprising the nonsilver elements of the optical train, including the reflectivity of two deformable mirrors at 93% each, two focal plane mirrors at 97% each, and one color filter at 60% transmission. The T_{all} curve is the product of all the above transmission factors.

$$T_{all}(\lambda) = QE(\lambda) \times R_{32}(\lambda) \times T_{area} \times T_{fil}.$$

This transmission factor is independent of a coronagraph's diffraction terms, listed in Sec. 4.2.

4.2 Transmission Factors Versus Angle

There are three types of star-planet angle-dependent transmission factors to be considered for each coronagraph design, as shown in Fig. 5 for HLC, SPC, and PIAACMC. These are the solid-angle factor Ω (arc sec^2), a point-source transmission factor T_{point}, and a diffuse-source transmission factor $T_{diffuse}$. In the present study, we assume that a single polarization of light is selected prior to detection for the HLC and PIAACMC coronagraphs, for the reason that the contrast is degraded by a factor of at least 3 or 4 for unpolarized light compared to linearly polarized light, which is not acceptable. On the other hand, for SPC, the factor is a more modest 1.5 to 2.0, which is more acceptable.
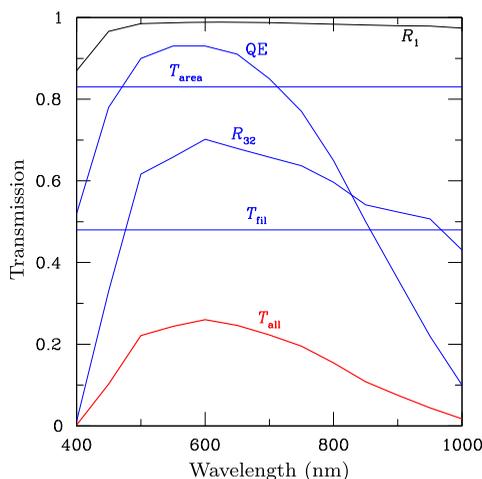

Fig. 4 Transmission factors for the coronagraphs on WFIRST, showing the wavelength dependence of quantum efficiency and mirror reflectivity, and the nominal wavelength independence of the secondary blockage and filter terms.
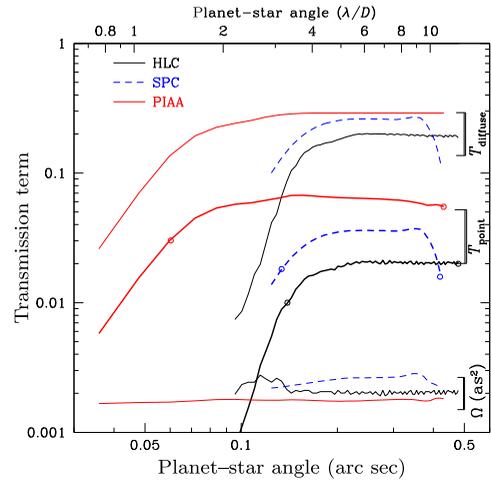

Fig. 5 Transmission factors for all three coronagraphs, as a function of planet–star separation. The design wavelength is 550 nm, so for other wavelengths, the planet–star axis must be scaled proportional to wavelength. The bottom group, Ω (square arc-second, as^2), is the projected solid angle on the sky of the FWHM of the PSF. The middle group, T_{point}, is the transmission factor for point sources, and the upper group, $T_{diffuse}$, is the transmission for a diffuse source, here the solar system zodi. The T values are for single polarization for HLC and PIAACMC, and unpolarized light for SPC.

The upper scale in Fig. 5 indicates the planet–star separation in units of λ/D, where $\lambda = 550$ nm is the design reference wavelength and $D = 2.37$ m is the design reference telescope diameter, so that $\lambda/D = 1$ is an angle of 0.04787 arc sec. For other wavelengths, we scale the curves in Fig. 5 by λ, so, for example, at longer wavelengths, the curves shift toward larger angles in arc sec units, and the PSF area increases (as λ^2). We discuss the resulting transmission factors in the present section.

4.2.1 Solid-angle factor Ω

The solid-angle factor Ω (arc sec^2) is shown near the bottom of Fig. 5. This is the solid angle subtended by the area within the FWHM of the PSF in the focal plane, for the design wavelength of the coronagraph (550 nm), and thus is the effective area of a point source (e.g., a planet) on the detector. For a clear-aperture telescope of diameter D, the angular FWHM is given by FWHM $= 1.03\lambda/D$; for example, for $\lambda = 550$ nm and $D = 2.37$ m, this gives FWHM $= 0.049$ arc sec, and the solid angle is 0.0019 arc sec^2. This nominally agrees with the plotted value for PIAACMC. The values for SPC and HLC are larger, as expected owing to additional pupil-plane obscurations, and slightly dependent on the location of the image.

In this simulation, we assume that the plate scale is set such that the shortest wavelength to be imaged is Nyquist sampled, with two detector pixels per FWHM of the PSF. Longer wavelengths will produce proportionately larger images, a consideration when detector noise is estimated (Sec. 4.7).

4.2.2 Point-source factor T_{point}

For the clear-aperture case, the fraction of incident light from a point source that falls within the solid angle of the FWHM is 0.4749, i.e., slightly less than half of the light (Ref. 30, Sec. 8.5.2). For the WFIRST pupil, and for light that is affected

by the coronagraph, i.e.,within the dark-hole region, the PROPER model gives the corresponding transmission factors labeled T_{point} in Fig. 5. We see that T_{point} is ∼0.06 for the PIAACMC system, which is a factor of 8 less than the clear-aperture ideal. Part of this (a factor of 2) is because a single polarization is assumed for PIAACMC, and another part is caused by stops inserted into the PIAACMC beam to keep uncanceled light from striking the dark-hole region. Simulations suggest that the remainder of the loss, up to a factor of 4, is caused by the action of the deformable mirrors in compensating for the spider-induced gaps in the wavefront. The values shown are referenced to the unblocked pupil area, so they do not include the T_{area} factor from Fig. 4.

The T_{point} value for the SPC case is for unpolarized (natural) light, so on the basis of polarization, it should be a factor of 2 larger than the PIAACMC value, but of course the SPC has a large part of its area blocked in the pupil, which drives the transmission factor down below that of PIAACMC.

For HLC, the T_{point} factor (∼0.02) is for a single polarization, which drives it down from an ideal 0.4749 by a factor of 2 to start, but in addition, part of the pupil is masked to achieve a deep dark hole, and furthermore, as was mentioned earlier, the combined action of the deformable mirrors apparently throws a lot of the planet light out of the image.

We expect that the described deformable mirror-induced losses would be smaller if the spider arm widths were smaller. However, we have not pursued this issue because the spider arms are not an adjustable parameter here, although it is obviously a rich topic for study for other types of space telescopes.

On each of the T_{point} curves in Fig. 5, we denote the nominal IWA by a small circle, determined by the rule of thumb as the angle at which the nominal transmission drops by a factor of 2. Clearly, there is a range of angles smaller than the indicated IWA, where the transmission is more reduced, but the coronagraph is still functioning. The question of how practical it will be to use any of the angular region inside the IWA remains to be studied.

A second small circle is used to indicate the effective outer working angle (OWA) for each coronagraph. This limit is set for each case by the angle at which the dark hole is no longer dark and the speckles start to become quite bright. The theoretical maximum angle of the OWA is about $(N/2)\lambda/D$, where N is the number of pistons across the deformable mirror. For $N = 48$ here, we find the maximum OWA to be 24×0.047 or 1.13 arc sec, which is much larger than the value of ∼0.5 arc sec shown in Fig. 5. The reason for this is probably twofold: first, the $N/2$ factor is an overestimation based on the assumption that only sine or cosine waves are needed, whereas in reality, both are needed, which leads to a factor of $N/4$, giving an OWA of 0.57 arc sec; second, in the design of these coronagraphs, it is likely that the designers sacrificed some OWA in order to gain a smaller IWA and/or a deeper dark hole, recognizing that there are more planets at small angles than at large angles.

In summary, future iterations of these coronagraphs are likely to produce improvements of these curves, but at this point, the largest potential improvement would come from regaining the factor of 2 loss owing to using a single polarization for HLC and PIAACMC. This assumes that the other polarization image is not of high quality, even though it will be recorded in parallel. If the coronagraph designs could be made to be less sensitive to polarization, or if a polarization compensator plate could be devised, we could gain back that factor of 2 loss of signal.

4.2.3 Diffuse-source factor $T_{diffuse}$

In addition to point sources of light (e.g., star, planet, exo-zodi), there is a diffuse source, the local zodi, that needs to be accounted for on the detector. At first glance, it might be thought that the local zodi is simply a collection of many individual, independent point sources, which is true. However, it is not true that it should be treated the same as a point source in tracking the flow of light toward the focal plane, because the light from a given point source falls on the focal plane both within the FWHM solid angle Ω (a small part) as well as outside that area (a large part). We assume here that the net effect of this broad distribution of many independent elements of a widely diffuse source is that the flux falling within a given Ω is more than would be expected from a simple sum of point sources using the aforementioned T_{point} factor. In particular, we assume that the intensity from a diffuse source will be limited by the transmission factor of the pupil stops alone, and not affected by the image plane stops (which largely impact mainly the on-axis star). Thus, we show in Fig. 5 the transmission factors labeled $T_{diffuse}$, and these curves are used solely to account for the contribution of the local zodi, which is truly diffuse. This means that the local zodi is added with a greater weight than the same zodi if placed around a distant star, and the net effect is to add a constant background signal in addition to the corresponding photon-counting noise.

4.3 Speckle Contrast Versus Angle

As a wavefront of a given photon passes through the optical system, it encounters (polarization-dependent) transverse variations of phase and amplitude, and each Fourier component of these variations gives rise to the probability that the photon will end up being diffracted in a direction outside the nominal solid angle Ω where the point-source-like image is located. These diffracted photons form a distribution of faint pseudo images across the dark hole, which we call speckles.

In the present simulation, the intensity and spatial distribution of speckles is estimated by assuming, from experience, a PSD, which describes the phase and amplitude distribution, in a statistical sense. We further assume that the deformable mirrors are driven to scatter additional starlight onto the locations of these speckles, but with an opposite phase, thus canceling the net electric field at each point in the dark hole to the maximum extent possible. The resulting speckle intensity is then averaged in azimuth, giving the speckle–star contrast factor C_{spec} as a function of planet–star separation, and shown for each coronagraph in Fig. 6.

A second factor that is taken into account in Fig. 6 is spacecraft pointing jitter. It is known that momentum wheels have slightly imperfect balance, so that as they rotate, even at constant angular speed, the spacecraft moves in opposition, resulting in a variation of the space direction of the optical axis of the telescope, with a frequency equal to that of the wheel. In addition, the spacecraft structure can respond in its resonant modes, resulting in additional pointing errors. The net result is that a star image will be displaced with respect to its intended position, and some extra light will leak past the coronagraph. The situation is simulated by summing the results of a distribution of stellar offsets. See Ref. 31 for a discussion of the expected pointing
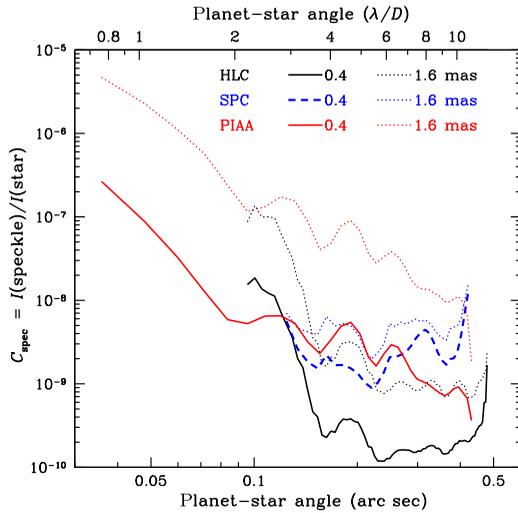
Fig. 6 Contrast of speckles in the dark hole for each coronagraph, for a small residual jitter (0.4 mas RMS) and a large residual jitter (1.6 mas RMS), at the design wavelength of 550 nm. For other wavelengths, the planet–star angle is replaced by one that is wavelength scaled, as suggested by the λ/D axis at the top.

jitter amplitudes and frequencies, and Ref. 28 for a discussion of the speckle simulations. We assume that the intrinsic jitter level of the spacecraft is 14 mas RMS per axis, with a Gaussian distribution. The motion of the star image is suppressed by a low-order wavefront sensing and control system,[32] resulting in a residual, uncompensated jitter level that is expected to be bounded by ∼0.4 mas RMS at the low end, and by ∼1.6 mas RMS at the high end. Note that the star is assumed to have a diameter of 1.0 mas (e.g., the Sun at 10 pc), which means that it is not worthwhile to suppress the pointing jitter to much less than 0.5 mas RMS.

In this paper, the expected speckle contrast levels C_{spec} for two bounding cases are shown in Fig. 6 as thick lines for the good (0.4 mas) case and as thin lines for the bad (1.6 mas) case. Notice that the good and bad cases are separated by about a factor of 2.5 for the SPC, indicating that it is relatively immune to pointing jitter. The good and bad cases for HLC are separated by a factor of ∼7, and for PIAACMC, the separation is about a factor of 20, indicating increased sensitivity to uncompensated pointing jitter.

In Fig. 6, as in Fig. 5, the curves for C_{spec} are drawn for 550 nm and 2.37 m diameter, so for longer wavelengths, for example, the curves shift to larger values of angle in arc sec units. The practical effect is that for longer wavelengths, we lose the ability to measure planets at smaller angles, but gain an ability to see planets and disks that might lie at larger angles from the star.

4.4 Target Count Rates

We start by estimating the count rate n_{star} (electrons per second) from a target star of magnitude $m_{star}(\lambda)$. If the telescope is pointed slightly away from the target star, so that the star falls within the area where the dark hole would normally be located, the count rate from the star will be

$$n_{star} = f(\lambda, m_{star}) \times BW \times A \times T_{all} \times T_{point} (elec/s),$$

where $f(\lambda, m_{star})$ is the star flux [photons/(s nm cm^2)] from Sec. 2.2, BW = $\Delta\lambda$ (nm) is the spectral bandwidth, A (cm^2)

is the collecting area of the telescope, T_{all} (electrons/photon) is the optical efficiency of the system, and T_{point} is the fraction of light contained within the FWHM of the PSF, from Sec. 4.2. Note that we count only that fraction of the starlight that falls within the FWHM of the image, as a simple approximation that recognizes that the background speckles have shapes similar to astrophysical point sources. The portion of the image outside this boundary is not as likely to be useful in detection as it would be if the background were flat.

The planet count rate n_{pl} is then given by the count rate of the star times the contrast factor (planet/star), from above, giving

$$n_{pl} = n_{star} \times C(\alpha)(elec/s)$$

in the area enclosed by the FWHM of the PSF.

4.5 Background Count Rate from Zodiacal Light

The total background count rate from the sky is the sum of intensities from speckles and local zodi plus exo-zodi, in this section. (In this study, we ignore scattered and diffracted contributions from companion stars.)

For a representative value, we define one zodi to have a brightness of

$$m_z = 22.7 (mag/arc sec^2),$$

which is the apparent brightness of the solar system's zodiacal light, at a wavelength of 500 nm, for an observer at a radial distance of 1 AU, in the dust symmetry plane, looking at an ecliptic longitude of 90 deg from the Sun, and at an ecliptic latitude of 20 deg (HST, ACS Instrument Handbook, Cycle 21, interpolated from Table 10.4). We further assume that this value is independent of wavelength and polarization. (In a DRM simulation with specific stars and pointing directions, the brightness, color, and polarization of the solar system zodi should be taken into account.)

For the current simulation, we assume that the solar system zodi brightness is a factor num$_{ss}$ = 1 times brighter, giving a count rate in the focal plane of

$$n_{ssz} = num_{ss} \times \Omega \times f(\lambda, m_z) \times BW \times A \times T_{all}$$
$$\times T_{diffuse}(elec/s).$$

For the external zodi, we use a model adopted by Ref. 33 from a numerical simulation by Kuchner (Ref. 34, Appendix A), which gives the brightness as

$$m_{ext} = 22.1 + 5.6 \times \log_{10}(R_{AU})(mag/arc sec^2)$$

for a statistically averaged inclination of 60 deg, where R_{AU} is the radius in AU units, in the plane of the disk. This relation is in agreement with the one zodi value given above, after accounting for the geometry, within ∼20%. It is sufficiently accurate for present purposes. The 5.6 factor corresponds to a brightness fall-off as $1/r^{2.24}$ (from $0.4 \times 5.6 = 2.24$), which is slightly faster than a $1/r^2$ law. The model extends from ∼0.4 to 5 AU, at which point it encounters the Edgeworth-Kuiper belt and is approximately flat to beyond 50 AU.

Using the relation for the magnitude m_{ext} of the external zodi, we find that the count rate n_{ext1} in the focal plane, for a zodi disk identical to the solar system disk, is

$$n_{\text{ext1}} = \Omega \times f(\lambda, m_{\text{ext}}) \times \text{BW} \times A \times T_{\text{all}} \times T_{\text{point}}(\text{elec/s}),$$

where we use the transmission factor T_{point}, per the discussion in Sec. 4.2. Then, assigning a factor of num_{ext} as a scaling factor in order to multiply the model by that number of external zodis, we find the count rate from the scaled external zodi to be

$$n_{\text{ext}} = \text{num}_{\text{ext}} \times n_{\text{ext1}}(\text{elec/s}).$$

We assume $\text{num}_{\text{ext}} = 6$ in this study. This corresponds to a factor of 2 for viewing the external disk from the outside rather than from the mid-plane (as for the solar system zodi) times an overall factor of 3. The latter scaling factor makes the exo-zodi cloud three times the optical thickness of the solar system disc, a factor chosen simply to make sure that we do not underestimate the disk flux.

4.6 Condition for Disk to Match Planet

It is of interest to ask, for each RV planet, what disk brightness is needed to make the disk signal equal the planet signal? Knowing this value will give us an idea of (1) how much disk background can be tolerated before the planet signal begins to be obscured by the disk, as well as (2) how bright a disk we can expect to detect around a star similar to the RV target star, given that we already have established that we could detect a planet around that star. We reserve for a future study an analysis of disk detection in the general case.

Let $\text{num}_{\text{equiv}}$ be the equivalent number of zodis needed in order for the disk signal to equal the planet signal. Using the results of Secs. 4.4 and 4.5, we find

$$\text{num}_{\text{equiv}} = n_{\text{pl}}/n_{\text{ext1}}(R_{\text{AU}}),$$

where we write $n_{\text{ext1}}(R_{\text{AU}})$ to emphasize that the evaluation is to be carried out at the semimajor axis location of the planet.

4.7 Background Count Rate from Speckles

The count rate n_{spec} from speckles, in the FWHM solid angle Ω on the detector, is given by

$$n_{\text{spec}} = n_{\text{star}} \times C_{\text{spec}}(\text{elec/s}).$$

To gain some perspective, a simple but very useful picture of the origin of speckles in a coronagraph is to imagine that the nearly perfect but nevertheless slightly irregular wavefront across the pupil of a telescope is decomposed into a sum of sine and cosine waves, each with an RMS amplitude of about h (nm). Also, recall that each of these waves will diffract a small amount of starlight as a diffraction grating does, giving us a sea of speckles. A rough estimate[16] of the resulting contrast (average speckle brightness divided by star brightness) across the image plane is $C_{\text{spec}} = \pi(4h/N\lambda)^2$, where N is the number of actuators per diameter, which can be used to correct the wavefront. The contrast is measured within the dark hole, out to an OWA of about $(N/2) \times (\lambda/D)$, where D is the effective diameter of the telescope and $N = 48$. This estimate tells us that to achieve $C_{\text{spec}} = 10^{-9}$, we need to have $h = 1$ Angstrom or 0.1 nm or 100 pm, RMS roughness across the corrected wavefront.

For the present study, a much more detailed simulation was performed, using expected values of surface (phase) and reflectivity (amplitude) errors of all optical elements, additional wavefront distortions owing to polarization effects, and an estimate of how well the deformable mirrors could correct the net phase and amplitude errors of the propagated wavefront. At each angular distance from the star, the resulting scattered light intensity in the focal plane was averaged over azimuth angle and expressed as a contrast value as a function of angular radius. Given that the spatial RMS variation of speckles is approximately equal to the average speckle intensity, this resulting intensity distribution is treated as a background noise, against which the planet intensity is to be measured.

4.8 Total Count Rate

The total number of detectable electrons per second from the sky, n_{sky}, in the solid angle Ω is the sum of the planet (n_{pl}), solar system zodiacal light background (n_{ssz}), external zodi level (n_{ext}), and speckle background (n_{spec}) count rates:

$$n_{\text{sky}} = n_{\text{pl}} + n_{\text{ssz}} + n_{\text{ext}} + n_{\text{spec}}(\text{elec/s}).$$

The total measured number of electrons per second is the sum of the detected sky rate (above) plus detector contributions. An expression that includes CCD-type detectors as well as electron-multiplying CCDs[27] is as follows:

$$n_{\text{total}} = (n_{\text{sky}} + D_{\text{c}} \times m_{\text{pix}} + \text{CIC} \times m_{\text{pix}}/t_{\text{frame}}) \times \text{ENF}^2$$
$$+ (N_{\text{R}}/G)^2 \times m_{\text{pix}}/t_{\text{frame}}(\text{elec/s}),$$

where D_{c} is the dark count rate, CIC is the clock-induced charge, ENF is the excess statistical noise factor due to fluctuations in the multiplication process, N_{R} is the RMS value of the read noise, G is the gain of the EMCCD, and t_{frame} is the time per readout frame, assuming that there are many readout frames per integration time t, so the number of frames per integration is $n_{\text{frame}} = t/t_{\text{frame}}$. Typical values of all parameters are listed in Table 3.

Table 3 Astrophysical and instrumental parameters, and typical values, for detecting a typical exoplanet with the CGI on WFIRST, for CCD and EMCCD detectors, and the resulting integration times.

Parameter	Units	CCD typical value	EMCCD typical value
n_{pl}	elec/s	0.012	0.012
n_{zodi}	elec/s	0.012	0.012
n_{spec}	elec/s	0.010	0.010
m_{pix}	pixels	5	5
D_{c}	elec/(pixel s)	0.001	0.0005
N_{R}	RMS elec/(pixel frame)	3	16
t_{frame}	s	300	300
CIC	elec/(pixel frame)	0	0.001
ENF		1	1.414
G		1	500
t	s	33,000	14,000

4.9 *Noise Count Rates*

The noise in a measurement is contributed by two main sources: (1) statistical fluctuations in the number of measured electrons and (2) the uncertainty in subtracting the background, where the background can vary spatially (e.g., zodiacal light and speckles) and vary with time (e.g., speckle brightness changes owing to thermally induced optical path variations in the telescope). Our ability to reduce this noise is limited by the nature of the fluctuations and by the effectiveness of our postprocessing algorithm.

For noise source 1, the RMS noise N_1 (elec) after a total integration time t is

$$N_1 = (n_{\text{total}} \times t)^{1/2} (\text{elec}),$$

which increases with time as the square root of time, since the noise is the statistical fluctuation of the number of collected electrons with time.

The statistics of speckles tells us that the spatial RMS variation in intensity is equal to the average value of the speckle intensity. The expected thermal variations of the optical paths within the telescope and coronagraph tell us that there also will be a time-varying component of speckle intensity. Using experience from ground and space observations, we expect that the total RMS variation could be reduced by postprocessing, by a factor f_{pp}, where $f_{\text{pp}} = 1/10$ is our adopted worst-case estimate, and $f_{\text{pp}} = 1/30$ is our adopted best-case estimate. So for noise source 2, the RMS noise N_2 (elec) after a total integration time t is

$$N_2 = f_{\text{pp}} \times n_{\text{spec}} \times t (\text{elec}),$$

which increases linearly with time because the total speckle counts increase linearly, and the noise is simply a scaled-down version of that total count.

Adding these statistically independent noise sources gives us the total noise, after postprocessing, at the location of a planet, as

$$N_{\text{total}} = (N_1^2 + N_2^2)^{1/2} (\text{elec}),$$

which increases with time at a rate that lies between square-root and linear, depending on the time-dependent factors in each of the noise sources.

4.10 *Signal-to-Noise Ratio*

The signal that we care about is S_{pl}, the number of collected electrons from the planet, in the total integration time t, where

$$S_{\text{pl}} = n_{\text{pl}} \times t (\text{elec}).$$

The ratio SNR of signal electrons to noise electrons is then

$$\text{SNR} = S_{\text{pl}}/N_{\text{total}},$$

which is dimensionless, but increases with time. Substituting from above, the SNR is

$$\text{SNR} = n_{\text{pl}} \times t / (n_{\text{total}} \times t + f_{\text{pp}}^2 \times n_{\text{spec}}^2 \times t^2)^{1/2}.$$

We adopt a detection criterion of a threshold SNR of a value of 5, so that

$$\text{SNR}_0 = 5.$$

Solving for the total integration time t, we find

$$t = \text{SNR}_0^2 \times n_{\text{total}} / [n_{\text{pl}}^2 - (\text{SNR}_0 \times f_{\text{pp}} \times n_{\text{spec}})^2] (\text{s}).$$

The term in the denominator, which contains f_{pp} (our postprocessing factor), is a consequence of our assumption that the noise from speckle subtraction is a fixed fraction of the intensity of the average speckle. This term has important implications for the minimum brightness of planet that can be detected, because it essentially gives us a noise floor, below which a planet with count rate n_{pl} (min) cannot be detected,

$$n_{\text{pl}}(\text{min}) = \text{SNR}_0 \times f_{\text{pp}} \times n_{\text{spec}} (\text{elec}).$$

By this criterion, integrations longer than t will not produce improved results. Note that with an SNR_0 of 5, and the best-case f_{pp} value of 1/30, the noise floor is set at 1/6 times the value of the average background speckle intensity in the neighborhood of the planet in the focal plane, which is an incentive to design a coronagraph mask producing faint speckles.

5 Radial-Velocity Planet Yield Estimates

Using the preceding formalism, we solve for the time required to achieve $\text{SNR}_0 = 5.0$. Note that the fixed noise floor forces the faintest planets to be impossible to image in a finite amount of time. No amount of integration will yield a detection of these planets. This (assumed) fixed noise floor is therefore an important limitation on our ability to image planets. The post-production factors are chosen based on our experience with subtracting PSFs from images from ground-based coronagraphs, as well as from HST images. A key focus of future work will be to substantiate and reduce this factor given more realistic simulations of the telescope's thermal response.

Once this procedure is completed for a given spectral band, we repeat it for all bands, here three bands (465, 565, and 835 nm) for the direct imaging channel, and three bands (660, 770, and 890 nm) for IFS. See Table 2 for the parameters of all bands. Typically, the short-wavelength bands produce most detections, owing mainly to diffraction, which places the response window at smaller angles for shorter wavelengths and therefore captures more planets, which tend to cluster at small angular separations.

For planets that are detectable (SNR > 5), we solve for the integration time under the ranges of assumptions regarding telescope jitter and postproduction factor. Planets that are detectable within a maximum integration time (1 day for imaging, 10 days for spectra) are retained. Finally, we generate a graphical display of the results in the form of a plot of contrast as a function of separation angle for detectable planets, and for each coronagraph architecture and spectral band. The resulting number of detectable RV planets is summarized in Table 4, for each coronagraph and continuum band. The total time to observe all three bands is given, assuming that the 565-nm band is used for initial detection, requiring one snapshot each for HLC, but two for PIAACMC and three for SPC, and then one snapshot each for the remaining bands, once the position angle of the planet is known.

A brief summary of the overall performance of the three architectures is shown in Table 5. A popular way to indicate the angular range of a coronagraph is to give IWA and

Table 4 Number (*N*) of RV planets detected by each coronagraph, in each of three spectral bands, assuming a single polarization for HLC and PIAACMC, and unpolarized light for SPC. The total time for detections in all three bands is indicated.

Coron.	N (465)	N (565)	N (835)	Total time (days)
HLC	15	15	3	8
SPC	13	15	4	14
PIAACMC	80	91	28	53

Table 5 Representative values of the angular range of each coronagraph architecture, and expected values of planet contrast, 5-sigma floor contrast, best case ($f_{pp} = 1/30$, and jitter = 0.4 mas RMS per axis) and integration time for $SNR_0 = 5$, for a typical planet.

			47 U Ma c: a typical planet		
Coron.	Innermost planet (mas)	Outermost planet (mas)	Contrast of planet (E-10)	Contrast of floor (E-10)	Integration time (h)
HLC	110	430	59	0.2	0.9
SPC	140	430	59	2.0	0.5
PIAACMC	40	430	59	3.4	0.2

OWA; however, these numbers can be misleading because detection is not a simple binary function of angle; for some architectures, the contrast drops smoothly through the inner parts of the dark region (see Fig. 5). Instead, we show a practical example of the range, using the known RV planets, in columns 2 and 3, where the angular separation of the closest and farthest detectable planet from the parent star is listed. Likewise, the best achievable contrast can be a misleading value, as the contrast floors of the architectures here typically vary by a factor of up to ~100. Instead, we quote in Table 5 a common example target, 47 UMa c, which has a planet/star contrast of 5.9×10^{-10}, at an angle of 242 mas, and can be detected by all three architectures. See Fig. 7 for a graphical simulation

of the 47 UMa b,c system with a 30-zodi disk for illustration, which is brighter than the 3-zodi disk used in the yield estimates in this paper. The table gives the 5-sigma sensitivity limit (contrast floor) for each example, and the integration time. It is clear from this table that these parameters can vary over a large range in a practical case, so the nominal criterion is not these performance parameters per se; rather, it is the total number of planets that can be detected, as shown in the following sections.

5.1 Hybrid Lyot Coronagraph Results

The science-imaging yield of known RV planets that are detectable with the HLC, in the 565-nm band (15%), for a single polarization (triangles), is shown in Fig. 8. The short-dash line (lower curve) is the 5-sigma speckle noise detection floor for the best case, which is a telescope pointing jitter of 0.4-mas RMS residual uncorrected angle, and a postprocessing factor of 30 times reduction in the spatial RMS speckle noise. The worst case (upper long-dash line) is similar, but for a pointing jitter of 1.6 mas and a postprocessing factor of only 10. The HLC has a 360-deg azimuth field, in a single snapshot. The IWA and OWA are effectively set by the angle limits of the floors as plotted. The solid triangle symbols are detections that can be carried out with the worst-case floor (upper); the open triangles are the extra planets that are detectable for the best-case floor (lower). For the HLC case shown, we expect to image about 15 RV planets, in a total integration time of 3 days, with an SNR of 5.0, in a single polarization, in this band, with an integration time of less than a day for each planet.

5.2 Shaped Pupil Coronagraph Results

The science-imaging yield of RV planets with the SPC is shown in Fig. 9. Here the science yield is 15 RV planet detections, each of which could be done in less than a day if the position angle of the planet was known. However, because it is not known, and because the SPC can only observe an azimuth range of
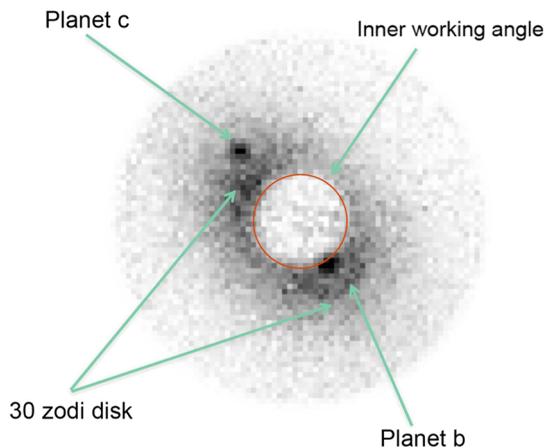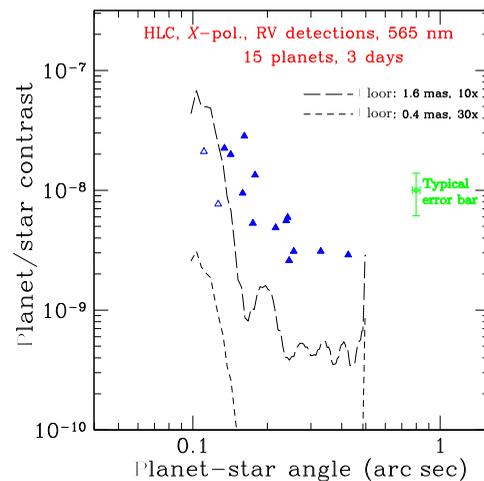

Fig. 7 Simulated WFIRST-AFTA coronagraph image of the star 47 Ursa Majoris, showing two directly detected planets (from Ref. 1), for HLC, and with a field of view radius of 0.5 arc sec. A PSF reference has been subtracted, improving the raw contrast by a factor of 10.

Fig. 8 Science imaging yield of known RV planets with HLC. Solid symbols are RV planets detectable with HLC in a 15% band centered at 565 nm, in less than a day each, in a single polarization, with a signal strength greater than the worst-case floor (long-dash line, 1.6 mas RMS pointing jitter, and a postprocessing factor of 1/10). The open symbols are for the additional detections possible with the best-case floor (0.4 mas jitter, 1/30 factor). Typical relative uncertainties in contrast and separation (Sec. 2.4) are indicated.
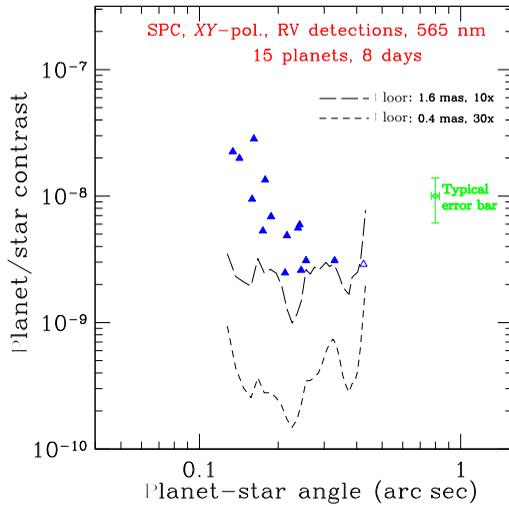
Fig. 9 Science imaging yield of known RV planets with SPC. Solid symbols are RV planets detectable with SPC in a 15% band centered at 565 nm, in less than a day each, in both polarizations simultaneously, with a signal strength greater than the worst-case floor (long-dash line, 1.6 mas RMS pointing jitter, and a postprocessing factor of 1/10). The open symbol is for the additional detection possible with the best-case floor (0.4 mas jitter, 1/30 factor). Typical relative uncertainties in contrast and separation (Sec. 2.4) are indicated.

~120 deg per snapshot, it will take three such snapshots to cover the full azimuth range; therefore, the total observing time will be about 8 days. Once a planet is discovered, the SPC can then be set at an appropriate azimuthal orientation for subsequent snapshots, either to improve the SNR or to observe at a different wavelength. Another difference with respect to the HLC is that the SPC has a higher contrast floor, which will reduce the number of detectable planets when searching for new discoveries, which are fainter than the RV planets indicated. A compensating factor is that the SPC is less sensitive to telescope jitter, which gives it a better performance margin in flight. Another compensating factor is that the SPC is less sensitive to polarization effects, so both polarizations can be observed simultaneously. The baseline for WFIRST-AFTA is to use the HLC for initial discovery at short wavelength and the SPC for long-wavelength characterization, even though Fig. 9 shows the SPC at a shorter wavelength, for the sake of uniformity in this paper.

5.3 PIAACMC Results

The science imaging yield of the backup architecture, the PIAACMC, is shown in Fig. 10. This architecture has the advantage (Figs. 5 and 6) of a greater overall throughput as well as a theoretically smaller IWA, allowing it to access more planets close to their star. However, an accompanying disadvantage is that it is more sensitive to telescope jitter, which in combination with the adopted values of jitter produces higher 5-sigma floor contrasts, as indicated in the figure. Therefore, many planets that were detected by a large contrast margin with the HLC or SPC are now closer to the PIAACMC contrast limit and will therefore require the best possible operating conditions (lowest jitter and most aggressive postproduction factor). Also, this version of PIAACMC has only one deformable mirror; hence, the azimuthal field is 180 deg, so two snapshots are required in order to fully examine a new system. The higher throughput and smaller IWA result in a greater number of detectable RV planets, and at
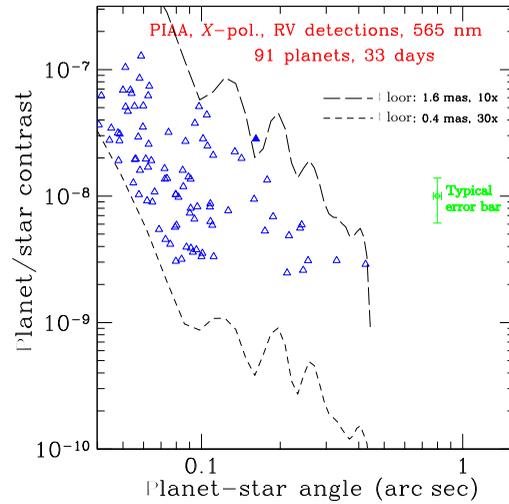

Fig. 10 Science imaging yield of known RV planets with PIAACMC. The solid symbol is for the single RV planet detectable with PIAACMC in a 15% band centered at 565 nm, in less than a day each, in a single polarization, with a signal strength greater than the worst-case floor (long-dash line, 1.6 mas RMS pointing jitter, and a postprocessing factor of 1/10). The numerous open symbols are for the additional detections possible with the best-case floor (0.4 mas jitter, 1/30 factor). Typical relative uncertainties in contrast and separation (Sec. 2.4) are indicated.

a faster rate per planet than for the HLC or SPC, but operating with a relatively smaller margin.

5.4 Top-Ranked Radial-Velocity Planets

All RV planets in Figs. 8–10, with angular separations >0.10 arc sec, are listed in Table 6. Explicit planet names, masses, radii, periods, and semimajor axes are listed, along with host star magnitudes. Each planet's separation and contrast at a phase angle of 72.77 deg is listed, as discussed in Sec. 2.3. For the 565-nm band, the integration times for each of the HLC, SPC, and PIAACMC coronagraphs are given for each detectable planet.

6 Radial-Velocity Planet Spectra Estimates

The CGI will use SPC for IFS spectra in the 660-, 770-, and 890-nm bands, at a spectral resolution of ~70. The value of $R = 70$ is chosen to approximately match the FWHM of the spectral features of Jupiter and Saturn, as shown in Fig. 2, where the individual spectral elements are indicated by the distance between tic marks on the three spectral channels drawn as S660, S770, and S890. It can be seen by eye that these channels are a good match to the narrow spectral features; therefore, these represent the optimum sampling of a noise-limited spectrum. We note that, by coincidence, $R = 70$ is also the recommended minimum resolution for an Earth-imaging coronagraph, as it approximately matches the width of the Earth's oxygen band at 760 nm, for the case where the P and R branches of this band are combined in a single spectral element; however, the approximate equality of these two resolutions is a complete numerical coincidence.

Two factors govern the yield of spectra: first, the IWA moves outward as the wavelength increases, cutting off planets that are too close to their star; second, the quantum efficiency of the detector decreases at longer wavelengths. All spectra will be in the unpolarized mode.

Table 6 All detectable RV planets with angular separations >0.10 arc sec, in the 565-nm band, for each coronagraph. The integration times are in days. The ordering is from large to small separation angles.

No.	RV planet name	Sep (as)	Contrast	t (days) HLC	t (days) SPC	t (days) PIAACMC	V (mag)	Mass (Jup)	Rad (Jup)	Per (days)	sma (AU)
1	55_Cnc_d	0.424	2.9E-09	0.36	0.43	0.08	5.96	3.54	14.1	4909	5.47
2	mu_Ara_c	0.329	3.1E-09	0.10	0.06	0.02	5.12	1.89	14.2	4206	5.34
3	HD_217107_c	0.257	3.1E-09	0.45	0.24	0.09	6.17	2.62	14.2	4270	5.33
4	HD_114613_b	0.245	2.6E-09	0.09	0.05	0.02	4.85	0.51	12.9	3827	5.31
5	47_UMa_c	0.243	5.9E-09	0.04	0.02	0.01	5.03	0.55	13.2	2391	3.57
6	HD_190360_b	0.239	5.6E-09	0.10	0.05	0.02	5.73	1.54	14.2	2915	3.97
7	HD_154345_b	0.216	4.9E-09	0.59	0.30	0.10	6.76	0.96	14.1	3342	4.21
8	HD_134987_c	0.212	2.5E-09	1.16	0.57	0.18	6.47	0.80	13.9	5000	5.83
9	HD_87883_b	0.188	6.9E-09	1.45	0.57	0.19	7.57	1.76	14.2	2754	3.58
10	upsilon_And_d	0.179	1.3E-08	0.01	0.00	0.00	4.10	4.12	14.0	1278	2.52
11	HD_39091_b	0.175	5.3E-09	0.13	0.06	0.02	5.65	10.09	11.7	2151	3.35
12	beta_Gem_b	0.162	2.8E-08	0.00	0.00	0.00	1.15	2.76	14.2	590	1.76
13	14_Her_b	0.159	9.5E-09	0.25	0.12	0.03	6.61	5.22	13.6	1773	2.93
14	47_UMa_b	0.143	2.0E-08	0.02	0.01	0.00	5.03	2.55	14.2	1078	2.10
15	gamma_Cep_b	0.134	2.2E-08	0.00	0.00	0.00	3.21	1.52	14.2	906	1.98
16	HD_192310_c	0.127	7.7E-09	0.59		0.02	5.73	0.07	5.0	526	1.18
17	HD_10647_b	0.111	2.1E-08	0.20		0.00	5.52	0.93	14.0	1003	2.02
18	HD_13931_b	0.111	3.3E-09			0.82	7.61	1.88	14.2	4218	5.15
19	HD_33636_b	0.110	5.9E-09			0.13	7.00	9.27	12.0	2128	3.27
20	HD_117207_b	0.108	6.3E-09			0.16	7.26	1.82	14.2	2597	3.74
21	HD_70642_b	0.108	8.7E-09			0.09	7.17	1.91	14.2	2068	3.18
22	HD_181433_d	0.108	8.2E-09			0.63	8.38	0.54	13.1	2172	3.02
23	GJ_676_A_b	0.105	2.5E-08			1.14	9.59	4.90	13.7	1057	1.82
24	GJ_649_b	0.105	4.4E-08			2.31	9.72	0.33	11.3	598	1.13
25	HD_128311_c	0.101	2.8E-08			0.03	7.48	3.25	14.1	924	1.75
26	HD_24040_b	0.101	3.5E-09			0.60	7.50	4.02	14.0	3668	4.92
27	HD_222155_b	0.100	3.3E-09			0.35	7.12	2.03	14.2	3999	5.14

To get an oversight view of the relative yield from each of the coronagraphs in this study, we show in Table 7 the number of RV planet spectra that could be obtained with the same configuration as for direct imaging, except that here the light is sent to an IFS, so that the only parameter changes are the central wavelengths (660, 770, and 890 nm) and the bandwidth (1/70 times the central wavelength). In addition, the pixel sizes at the IFS have been set so as to give Nyquist sampling at 600 nm, and the limit on observing time per target has been increased to

a maximum of 10 days per spectrum, although the average time in the table is ~2.5 days per spectrum. The assumed polarizations are the same as for imaging, i.e., single polarization for HLC and PIAACMC, but unpolarized for SPC.

7 Dust Disk Estimates

Disks already will have been included in the search for RV planets, as we cannot avoid seeing whatever disks are already there, within the limits of our integration time per target. For the fixed

Table 7 The number of $R = 70$ spectra of RV planets that could be obtained from each of the HLC, SPC, and PIAACMC coronagraphs, and the total observing time to obtain these spectra, with further details given in the text. The current plan is to use only the SPC for spectra.

Coron.	N (660)	N (770)	N (890)	Total time (days)
HLC	9	7	1	43
SPC	11	6	1	53
PIAACMC	56	45	21	226

solid angle of a pixel in the focal plane, the surface brightness of a disk is independent of target distance, but the angular size will scale as the inverse of distance. To give an indication of how disk and planet brightness terms are related, we use the relation in Sec. 4.6 for num_equiv to find the number of solar system type dust disks that would have to be placed around a target star in order to have the disk signal match the RV planet signal, in the FWHM of an angular resolution element. We find that the median number is roughly $num_{equiv} \sim 250$, meaning that it would take that many times the solar system disk density to equal the RV planet signals.

For perspective on this value of num_equiv, we note that the one result of the Keck interferometer search for zodiacal dust around nearby stars[35] is that the median zodi level is 12 ± 24 zodis, assuming a lognormal distribution. This means that from the perspective of detecting RV planets, we do not expect that dust disks will be a significant source of noise or confusion. On the other hand, from the perspective of being interested in measuring the dust disks themselves, this result suggests that the CGI may have to spend longer integration times for disks than

for RV planets to make meaningful detections. This topic of dust disk detection with CGI will be addressed more fully in a separate paper, as it is beyond the scope of the present study.

8 Mission Time Estimate

Starting with the integration times for RV planets given above, we can make a rough estimate of how the CGI could spend its 1-year allocation of time on the WFIRST-AFTA mission. There are five main categories to consider: (1) RV planet imaging, (2) RV planet spectra, (3) disk imaging, (4) new planet searches, 5)) general observer (GO) programs, and (6) overhead. A nominal time estimate for each of these categories is sketched below. Note that this is not a full DRM, but merely a notional allocation of coronagraph mission time.

8.1 Time for Photometry of Known Radial-Velocity Planets

The total time required for a first-time detection of an RV planet is determined in this study by the integration time assuming that the planet is in an approximately optimum orbital position. It is likely that we can predict the right time to observe an RV planet because we already will have the ephemeris from RV observations, with only the inclination of the orbit and the position angle as unknown factors. For the current work, we assume a statistical average inclination of 60 deg. For HLC, with a full 360 deg of azimuth in a single snapshot, only one snapshot of a target needs to be taken. Numerical simulations show that all of the RV planets can be detected on the first try if they are observed when they are in the orbital range from ∼45 to 90 deg, where 90 is maximum elongation. This range occurs ∼25% of the time, allowing for orbital symmetry. Most RV periods are in the range of 2 to 10 years, so the time when a planet is in an optimum orbital window is easily predicted, assuming that ongoing

Table 8 Nominal time allocation and performance against requirements for CGI, for each major category of observation. These values will be updated when detailed engineering overhead times are available, and a realistic DRM can be calculated.

L1 product	Requirement	Performance assessment	Inst.	Comment	Clock time (days)
Exoplanet images	>12 planets	15 RV planets in 30 days at 565 nm, x-pol. 15 RV planets in 4 days at 465 nm, x-pol 15 RV planets in 4 days at 565 nm, y-pol 3 RV planets in 2 days at 835 nm, x-pol	HLC	HLC meets requirements, with margin	40
Exoplanet spectra	>6 planets	11 RV spectra in 30 days, 660 nm, unpol. 6 RV spectra in 17 days, 770 nm, unpol. 1 RV spectrum in 6 days, 890 nm, unpol.	SPC	SPC meets requirements, with margin	53
Disk images	Several disks	During all imaging observations Additional 30 days dedicated to disks	HLC	Need detailed simulations	30
New planet searches	None	Expect ∼2.5 planets per star accessible range of radii and periods	HLC	Need detailed simulations	85
GO programs	25% of time	General observer projects	HLC, SPC	Community proposals	91
Overhead	None	16 days total for initial RV obs. ∼0.25 days per target, for ∼160 additional observations	HLC HLC, SPC	Setup times and stability need detailed simulations	56
Total time					**365**

Doppler measurements continually refine the orbital solution. The 40 days of clock time listed in the top part of Table 8 includes multiple filters and polarizations, as well as search time for the initial acquisition of the planet, and additional time to achieve better than the minimum SNR.

8.2 Time for Spectra of Known Radial-Velocity Planets

We use SPC and IFS for spectra in the 660-, 770-, and 890-nm bands, at a spectral resolution of ∼70, an SNR_0 value of 5, and assuming that the albedo in the near-continuum regions is the same value (50%) as at shorter wavelengths. An integration time limit of 1 week is assumed for spectra, greater than the 1-day limit for filter photometry, owing to the higher spectral resolution. Two factors govern the yield of spectra: first, the IWA moves outward as the wavelength increases, cutting off planets that are too close to their star; second, the quantum efficiency of the detector decreases at longer wavelengths. The net result is that we expect to obtain spectra of RV planets at the rates of ∼11 spectra in 30 days in the 660-nm band, 6 spectra in 17 days in the 770-nm band, and 1 spectrum in 6 days in the 890-nm band. All SPC spectra will be in the unpolarized mode.

8.3 Time for Disk Images

As noted in Sec. 7, disks are automatically included in the search for RV planets, adding no extra time for that aspect. However, we expect to conduct a deeper search for disks around some of the RV target stars as well as additional targets, for which we allocate 30 days of observing time, subject to a future study.

(1) For as-yet-undiscovered (new) planets, a precise estimate of search time requires a full DRM, which will be carried out in future phases. We initially allocate 85 days for this search. (2) The WFIRST mission allocates ∼25% of the time to a GO program, so for CGI, this would be 91 days. (3) We assume that we will need 1 day to set up the dark hole for each RV planet when observed for the first time. Then, for a given RV target, subsequent observations in a different polarization and with different filters should take less time to tune the dark hole, for which we assume a quarter-day each for ∼140 targetings. We also assume that the initial checkout of the spacecraft will consume 5 days of coronagraph time. We thus conservatively estimate a total of 56 days of overhead.

8.4 Total Time

Adding the aforementioned time allocations for CGI, we find a total of 365 days required for the proposed program, as shown in Table 8.

9 Summary

We find that the CGI on the WFIRST-AFTA mission is expected to produce dramatic advances in the science of exoplanets around nearby stars, in addition to being a technology pioneer instrument that will prepare for even more capable instruments on later missions. But even in their current preformulation phase, the coronagraph mask designs, tailored to the WFIRST-AFTA pupil, are demonstrating that known RV planets can be directly detected and spectrally characterized in sufficient numbers to provide first views of these planets not obtainable by any other means. In addition, the coronagraph will provide visible-light images of debris disks closer to their stars than heretofore available, giving us direct views of these objects and directly informing us of the degree to which dust can compete with planets in brightness and detectability. This excellent sensitivity to both planets and disks will give us a unique insight into the formation and evolution of planetary systems. Finally, although not demonstrated in this paper, we expect that the coronagraph will allow us to directly detect and characterize currently unknown planets around nearby stars, truly opening our eyes to these new worlds for the very first time.

References

1. D. N. Spergel et al., "WFIRST-AFTA 2015 report," (2015), http://wfirst.gsfc.nasa.gov/science/sdt_public/WFIRST-AFTA_SDT_Report_150310_Final.pdf (8 March 2016).
2. A. Burrows, "Scientific return of coronagraphic exoplanet imaging and spectroscopy using WFIRST," 22 December 2014, http://arxiv.org/abs/1412.6097 (8 March 2016).
3. R. Hu, "Ammonia, water clouds and methane abundances of giant exoplanets and opportunities for super-Earth exoplanets," 20 November 2014, http://arxiv.org/abs/1412.7582 (8 March 2016).
4. M. Marley et al., "A quick study of the characterization of radial velocity giant planets in reflected light by forward and inverse modeling," 7 January 2015, http://arxiv.org/abs/1412.8440 (8 March 2016).
5. G. Schneider, "A quick study of science return from direct imaging exoplanet missions: detection and characterization of circumstellar material with an AFTA or Exo-C/S CGI," 13 November 2014, http://arxiv.org/abs/1412.8421 (8 March 2016).
6. R. A. Brown, "True masses of radial-velocity exoplanets," *Astrophys. J.* **805**, 188 (2015).
7. W. A. Traub, "The colors of extrasolar planets," 2003, http://articles.adsabs.harvard.edu/cgi-bin/nph-iarticle_query?db_key=PRE&bibcode=2003ASPC..294..595T&letter=.&classic=YES&defaultprint=YES&whole_paper=YES&page=595&epage=595&send=Send+PDF&filetype=.pdf (8 March 2016).
8. K. Stapelfeldt et al., "Exo-C: imaging nearby worlds," 2015, https://exep.jpl.nasa.gov/stdt/Exo-C_Final_Report_for_Unlimited_Release_150323.pdf (8 March 2016).
9. S. Seager et al., "Exo-S: starshade probe-class," 2015, http://exep.jpl.nasa.gov/stdt/Exo-S_Starshade_Probe_Class_Final_Report_150312_URS250118.pdf (8 March 2016).
10. W. A. Traub et al., "A consistent analysis of direct imaging missions," (2016, in preparation).
11. C. Stark et al., "Maximizing the exoEarth candidate yield from a future direct imaging mission," *Astrophys. J.* **795**, 122 (2014).
12. R. A. Brown, "Science parametrics for missions to search for Earth-like exoplanets by direct imaging," *Astrophys. J.* **799**, 87 (2015).
13. E. Han et al., "Exoplanet orbit database. II. Updates to exoplanets.org," *Publ. Astron. Soc. Pac.* **126**, 827–837 (2014).
14. W. A. Traub, "An empirical mass-radius relation for exoplanets," (2016, in preparation).
15. M. J. Pecaut and E. E. Mamajek, "Intrinsic colors, temperatures, and bolometric corrections of pre-main-sequence stars," *Astrophys. J. Suppl. Ser.* **208**, 9 (2013).

16. W. A. Traub and B. R. Oppenheimer, "Direct imaging of exoplanets," 2010, www.amnh.org/content/download/53052/796511/file/DirectImagingChapter.pdf (8 March 2016).

17. E. Karkoschka, "Methane, ammonia, and temperature measurements of the Jovian planets and Titan from CCD-spectrophotometry," *Icarus* **133**, 134–146 (1998).

18. K. L. Cahoy, M. S. Marley, and J. J. Fortney, "Exoplanet albedo spectra and colors as a function of planet phase, separation, and metallicity," *Astrophys. J.* **724**, 189–214 (2010).

19. M. C. Noecker et al., "Coronagraph instrument for WFIRST-AFTA," *J. Astronom. Telesc. Inst. Syst.* **2**(1), 011001 (2016).

20. J. Trauger et al., "Hybrid Lyot coronagraph for WFIRST-AFTA: coronagraph design and performance metrics," *J. Astronom. Telesc. Inst. Syst.* **2**(1), 011013 (2016).

21. B. J. Seo et al., "Hybrid Lyot coronagraph for WFIRST-AFTA: occulter fabrication and high contrast narrowband testbed demonstration," *J. Astronom. Telesc. Inst. Syst.* **2**(1), 011019 (2016).

22. E. Cady et al., "Demonstration of high contrast with an obscured aperture with the WFIRST-AFTA shaped pupil coronagraph," *J. Astronom. Telesc. Inst. Syst.* **2**(1), 011004 (2016).

23. K. Balasubramanian et al., "WFIRST-AFTA coronagraph shaped pupil masks: design, fabrication and characterization," *J. Astronom. Telesc. Inst. Syst.* **2**(1), 011005 (2016).

24. E. Pluzhnik et al., "Design of off-axis PIAACMC mirrors," *J. Astronom. Telesc. Inst. Syst.* **2**(1), 011018 (2016).

25. B. Kern et al., "Phase-induced amplitude apodization complex mask coronagraph mask fabrication, characterization, and modeling for WFIRST-AFTA," *J. Astronom. Telesc. Inst. Syst.* **2**(1), 011014 (2016).

26. M. W. McElwain et al., "PISCES: an integral field spectrograph technology demonstration for the AFTA coronagraph," (2016, in preparation).

27. L. K. Harding et al., "Technology advancement of the CCD201-20 EMCCD for the WFIRST-AFTA coronagraph instrument: sensor characterization and radiation damage," *J. Astronom. Telesc. Inst. Syst.* **2**(1), 011007 (2016).

28. J. Krist, B. Nemati, and B. Mennesson, "Numerical modelling of the proposed WFIRST-AFTA coronagraphs and their predicted performances," *J. Astronom. Telesc. Inst. Syst.* **2**(1), 011003 (2016).

29. Quantum Coating Inc., http://www.quantumcoating.com/fss99 (8 March 2016).

30. M. Born and E. Wolf, *Principles of Optics*, 3rd ed., Pergamon Press, Oxford, U.K. (1965).

31. B. Kern, "Impact of WFIRST-AFTA line-of-sight jitter distributions on phase-induced amplitude apodization complex mask coronagraph science yield," *J. Astronom. Telesc. Inst. Syst.* **2**(1), 011016 (2016).

32. F. Shi et al., "Low order wavefront sensing and control for WFIRST-AFTA coronagraph," *J. Astronom. Telesc. Inst. Syst.* **2**(1), 011021 (2016).

33. W. A. Traub, "Zodi disc contrast," (2016, in preparation).

34. M. Kuchner, "Appendix A," 2006, https://exep.jpl.nasa.gov/files/exep/STDT_Report_Final_Ex2FF86A.pdf (8 March 2016).

35. B. Mennesson et al., "Constraining the exozodiacal luminosity function of main-sequence stars: complete results from the Keck Nuller mid-infrared survey," *Astrophys. J.* **797**, 119 (2014).

Wesley A. Traub has been the JPL project scientist for WFIRST since 2014, and before that, he was the chief scientist of NASA's Exoplanet Exploration Program for about 10 years. He earned his BS from the University of Wisconsin–Milwaukee in 1962 and his PhD in physics from the University of Wisconsin–Madison in 1968. He is the author of 185 refereed journal papers and has written three book chapters. His current research interests are exoplanet statistics, coronagraphs, star shades, and exoplanet spectroscopy.

James Breckinridge is a visiting associate at Caltech and was at JPL for 33 years. He earned his BSc from Case Institute and PhD from the University of Arizona. He was a member of the science team and instrument scientist for ATMOS. He led work on WF/PC2 for HST, and the spectrometers for Galileo and Cassini. He is the author of a book on Fourier transform spectrometers and another on basic optics for astronomical sciences.

Thomas P. Greene is an astrophysicist at NASA Ames Research Center, where he works on developing space observatories and conducts observations of young stars and extrasolar planets. He is a co-investigator on the NIRCam and MIRI science instruments of the James Webb Space Telescope and was a member of the WFIRST-AFTA Science Definition Team. He received his PhD in astronomy from the University of Arizona and his BA in physics from the University of California.

Olivier Guyon is an associate professor of optical sciences at the University of Arizona, an associate astronomer at the University of Arizona, and the Subaru Coronagraphic Extreme-AO project lead at the Subaru Telescope. He develops coronagraphs and wavefront control systems for space and ground-based telescopes, and his research is focused on high-contrast imaging techniques for identification and characterization of exoplanets.

N. Jeremy Kasdin is a professor at Princeton University in the Mechanical and Aerospace Engineering Department and vice dean of the School of Engineering and Applied Sciences. He received his BSE from Princeton University in 1985 and his PhD in 1991 from the Department of Aeronautics and Astronautics, Stanford University. After being the chief systems engineer for NASA's Gravity Probe B spacecraft, he joined the Princeton faculty in 1999, where he researches space systems.

Bruce Macintosh has been a professor of physics at Stanford University since 2013, and before that, he was a physicist at Lawrence Livermore National Laboratory. His received his PhD from UCLA. He is the principal investigator for the Gemini Planet Imager instrument and the GPI Exoplanet Survey. He works on direct detection and characterization of extrasolar planets.